Storm- and tide-induced infragravity dynamics at an intermediate-to-dissipative microtidal beach

Lorenzo Melito[1], Luca Parlagreco[2], Saverio Devoti[2]and Maurizio Brocchini[1]

[1]Department of Civil Engineering and Architecture (DICEA); Università Politecnica delle Marche, Ancona, Italy

[2]Italian Institute for Environmental Protection and Research (ISPRA); Rome, Italy

Key Points:

- Storms and tide are simulated with XBeach through an innovative calibration approach, to study infragravity waves at Sabaudia (Italy)
- Bound long waves grow in the shoaling zone and stop growing/decay in the surf zone, with no shoreline dissipation
- Albeit small, tidal excursion significantly alters onshore fluxes and reflection coefficients for intermediate IG frequencies

Corresponding author: Lorenzo Melito, `l.melito@univpm.it`

Abstract

Numerical simulations of a range of wave climates and tide conditions made with the model XBeach are exploited to study propagation, evolution, dissipation, and reflection patterns of infragravity waves (IGW) at the intermediate-to-dissipative beach of Sabaudia (Tyrrhenian sea, Italy). On the basis of a novel calibration process performed using field swash properties collected by a nearby monitoring station, the model reproduces swash characteristics with good skill (Willmott index of agreement $D = 0.61$–0.79). IGW at Sabaudia beach evolve exclusively as bound long waves (BLW) growing across the shoaling region for both mild and intense wave climate. BLW release occurs still in the inner shoaling zone and, thus, may not be strictly connected with wave breaking inception, as usually assumed. Furthermore, values of the dimensionless bed slope β_H at which transition from steep- to mild-slope behaviour occurs are higher that traditional threshold. Finally, although the small tide (0.4 m between MHWS and MLWS; tide range/breaking wave amplitude ratios between 0.14 and 1.1) does not alter bulk IGW reflection significantly, low tide is effective in reducing onshore IGW fluxes and, ultimately, reflection coefficients R^2 selectively for intermediate IG frequencies. Our study, for the first time, gives clear evidence that the tide has a role in determining frequency-dependent IGW dynamics and altering the dissipative state of a mild sloping beach also in a microtidal environment.

Plain Language Summary

Infragravity waves (IGW) are oscillations of the water level with typical periods of 20–30 seconds or more, and are relevant to a number of coastal processes, like beach inundation and mobilization of sand. A set of storm conditions and tidal levels is here simulated with a computer-based numerical model to observe how IGW evolve and dissipate at the beach of Sabaudia (Italy), characterized by low slopes and a small tidal excursion. It is found that IGW at Sabaudia develop and intensify thanks to a transfer of wave energy from the wind waves to the IGW itself. Upon entering the coastal region where waves break, IGW are set free to propagate and then stop growing or decay in intensity, due to increasing dissipation mechanisms occurring in shallow waters. The presence of IGW at Sabaudia is dominant, especially when intense storms occur. Although small in comparison to other beaches, the variation of tidal level at Sabaudia is capable of changing how much of the IGW energy is able to reach the emerged beach, mainly

for an intermediate range of IGW wave periods. Tide should therefore be taken into account when evaluating wave-related inundation, even in coasts when the tidal range is small.

1 Introduction

Infragravity waves (IGW hereafter) are low-frequency oscillations of the water surface with periods of 20–30 seconds to 5 minutes or more, mostly generated as either long-period oscillations forced by short wave groups (bound long waves, BLW; Longuet-Higgins & Stewart, 1964) or free waves triggered by cross-shore variation of the breakpoint due to differential breaking of waves within individual wave groups (breakpoint-forced long waves, BFLW; Symonds et al., 1982). Field and experimental investigations have ascertained the influence of IGW into a number of nearshore processes, such as sediment transport and subsequent morphological evolution of sandy beaches (Baldock et al., 2010; de Bakker et al., 2016), tidal inlet dynamics (Williams & Stacey, 2016; Bertin & Olabarrieta, 2016), swash and run-up characteristics (Ruessink et al., 1998; Ruggiero et al., 2001), dune erosion (Roelvink et al., 2009), and seiching (Okihiro et al., 1993). A thorough review of the features and dynamics of IGW is given in Bertin et al. (2018).

It is now acknowledged that IGW-related processes are frequency-dependent. Battjes et al. (2004) analyzed experimental data of waves propagating over a barred profile and concluded that the growth rate of IGW increases with increasing frequency, implying a dependence of the energy transfer from short to long (bound) waves. Field data examined by de Bakker et al. (2014) revealed a strong dissipation of high-frequency IGW, whereas low-frequency IGW show standing wave pattern, with increased IG reflection at the shoreline and minimal dissipation.

Also tide is shown to exert an influence over the amount of dissipation and reflection of infragravity energy on a coast. A tidal modulation of IGW reflection has been observed by, e.g., Okihiro and Guza (1995) and Bertin et al. (2020) with a larger reflection of IG energy at the shore during high tide than during low tide. This occurs because the sea level rise due to high tide allows waves to meet the shore at the upper portion of the intertidal beach, which is generally steeper than its lower part, especially in coasts with a considerable tidal range. A larger loss of IG energy over a (convex) low-tide surf

zone than over a (concave) high-tide surf zone has also been discussed by Thomson et al. (2006).

Most of the aforementioned conclusions on low-frequency waves evolution in the nearshore have been achieved mainly for meso- and macrotidal oceanic coasts, whereas the corresponding IG mechanisms emerging at microtidal beaches have been comparatively less studied. In this manuscript we present a study of infragravity-related dynamics at the mildly sloping, microtidal beach of Sabaudia (central Tyrrhenian sea, Italy). The relevant generation, dissipation, and reflection mechanisms of IGW are analyzed by means of the numerical model XBeach (Roelvink et al., 2009; Ruffini et al., 2020). The model is first calibrated using a novel approach that combines field observations of swash characteristics collected by a nearby monitoring station, and hindcast data from the freely available oceanographic model of the European Union Copernicus Marine Service. The approach consists of successive calibrations on the most relevant parameters, it is rather straightforward to apply and exploits only standard video products, making it appealing to use when hydrological field data are not available. The calibrated XBeach is then tested against a set of statistically significant synthetic storms covering a range of offshore wave heights, allowing for the study of IGW features across mild to extreme wave conditions. Our work contributes to improving our understanding of low-frequency wave dynamics at microtidal coasts typical of the Mediterranean basin. A description of the study site, wave climate features, and modelling set-up is given in Section 2. Results of the calibration process and IG analysis are given in Section 3 and discussed in Section 4. Concluding remarks are finally given in Section 5.

2 Materials and Methods

2.1 Study Site

The investigated beach lies within the municipality of Sabaudia (Lazio region, central Italy) and is part of the Circeo National Park, one of the oldest natural reserves in Italy. Located along the middle Tyrrhenian Sea, the Sabaudia coastline presents a NW–SE orientation and faces approximately 240° from the north (Figure 1a). The tidal regime in the area is microtidal and semi-diurnal with the tidal range rarely exceeding 0.5 m, and tide-related currents may be taken as negligible. Native sediment consists of medium-

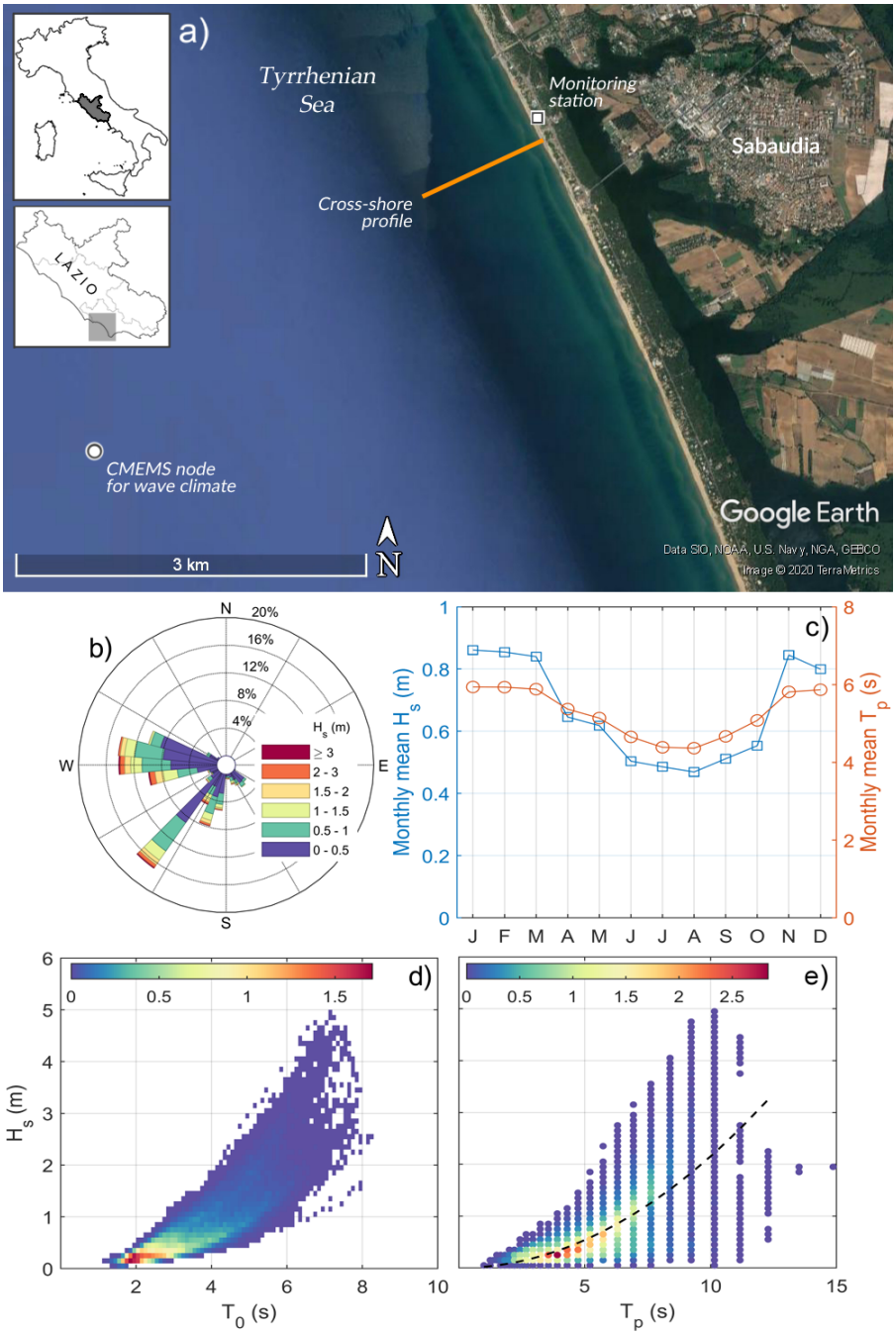

Figure 1. Geographical setting and hindcast wave climate (2006–2016) at Sabaudia. **a)** Map of the Sabaudia coast (picture adapted from Google Earth). Locations of the video-monitoring station, the cross-shore profile used for the numerical simulations, and the CMEMS model grid node for wave parameters extraction are shown. **b)** directional wave rose; **c)** monthly mean H_s (blue line) and T_p (orange line); **d)** joint probability distribution of H_s–T_0; **e)** joint probability distribution of H_s–T_p. The best fit regression line of Equation (1) is plotted with a dashed line.

to-fine sand with $d_{50} = 0.14$ mm at around 10 m depth, and $d_{50} = 0.3$ mm at the beach face (Parlagreco et al., 2019).

Based on 2006–2016 modelled wave statistics, the Iribarren number $\xi = \beta_s/\sqrt{H_0/L_0}$ (Battjes, 1974), with β_s being the mean surf zone slope, ranges between 0.2 and 1 for weak-to-moderate wave conditions ($H_s < 2$ m) but is consistently below 0.3, the threshold value for dissipative-state profiles (Stockdon et al., 2006; Soldini et al., 2013), for $H_s >$ 3 m. This qualifies the morphological state of the beach as intermediate-to-dissipative (Wright & Short, 1984), such state shifting towards the dissipative end of the spectrum with more intense waves.

The submerged beach usually presents two or three bars (Parlagreco et al., 2019). The outer bar is mostly linear whereas the inner bars show some sinuosity, typical of a Rhythmic Bar and Beach (RBB) morphology. The inner bars are occasionally interrupted by rip channels common for a Transverse Bar and Rip (TBR) state (Taramelli et al., 2020). Typical of the region are shoreward-propagating accretionary waves (SPAW) with displacement time scales of a few months or less, which are usually visible through monitoring products (Parlagreco et al., 2019).

2.2 Wave Climate

The lack of nearby wave buoys hinders the collection of *in situ* wave climate observations. To make up for this deficiency, wave data for the following analyses are obtained from the hindcast Mediterranean Sea Waves oceanographic model run by the EU Copernicus Marine Service CMEMS (Korres et al., 2019).

Hourly values of modelled significant wave heights H_s, mean (zero-crossing) wave periods T_0, peak periods T_p and main wave directions θ are collected for the period 2006–2016 at the model node with coordinates 41°.2708 N, 12°.9583 E, at around 77 m water depth, so that they can be assumed to be in deep waters. The same parameters are also collected for the period October 2017–March 2018, to be employed for the definition of XBeach wave input for the calibration stage.

A long-term wave climate characterization is given in Figure 1b–e. Wave attack is predominantly bimodal in the area, with waves coming from W and SW sectors (Figure 1b). The 10-year mean significant wave height is 0.66 m. Average wave parameters

Table 1. Significant wave height H_s, peak period T_p, and dimensionless fall velocity Ω for the six sample storms.

storm	S1	S2	S3	S4	S5	S6
H_s (m)	0.58	0.85	1.25	1.83	2.68	3.24
T_p (s)	5.21	6.30	7.63	9.23	11.17	12.28
Ω	6.7	8.1	9.8	11.9	14.4	15.8

show a marked seasonal variability in both wave height (monthly mean H_s up to 0.9 m in winter and around 0.5 m in summer months) and peak period (monthly mean T_p of 6 s in winter and 4.5–5 s in summer; Figure 1c).

Estimated 10-year joint probability distributions of H_s–T_0 and H_s–T_p are given in Figure 1d–e. In Figure 1e is also plotted the best fit curve of the dataset H_s–T_p, which gives the following site-specific empirical relation:

$$H_s = \left(\frac{T_p}{6.818}\right)^2 \quad \text{or} \quad T_p = 6.818\sqrt{H_s} \tag{1}$$

with $R^2 = 0.56$ significant at the 95% level. Equation (1) is used to define six statistically representative storms, which are later used to evaluate long-wave transformation and beach response as a function of wave climate intensity (Section 3). H_s and T_p for the sample storms are collected in Table 1, along with the respective dimensionless sediment fall velocity Ω. All selected storms belong to lower-intermediate-to-dissipative states for the investigated beach ($\xi \approx 0.23$ and Ω above the threshold value of 6; Wright and Short (1984)) and are therefore suitable for a numerical study of wave evolution where breaking-related processes are involved.

The influence of tidal stage on infragravity energy fluxes is also investigated in this work. For this purpose, mean high water spring (MHWS) and mean low water spring (MLWS) levels are extracted from a 3-year tidal record from the nearby tide gauge at Anzio, about 36 km north-west of Sabaudia (*Website of the Italian Tide Gauge Network*, 2021), and given as uniform initial water level for the sample storms in Table 1, allowing simulation of different tidal stages. MHWS and MLWS levels of +0.2 m and −0.2 m are obtained, respectively, confirming the microtidal nature of the investigated coast.

2.3 Video-monitoring Products and Post-processing

The beach of Sabaudia and the surrounding coast are being monitored since 2015 by a video-monitoring facility installed and maintained by the Italian Institute for Environmental Protection and Research (ISPRA). The monitoring station captures snapshots of the nearshore and produces typical products such as time exposure (timex) images, commonly used to track the evolution of submerged sand bars (Lippmann & Holman, 1989; Holman et al., 1993), and timestack images which can be profitably employed to study swash processes (Aagaard & Holm, 1989).

For the present application, swash properties at Sabaudia are extracted and employed to calibrate the model (see Section 2.4). Timestacks are analyzed to extract 15-minute time series of the instantaneous shoreline at a mean frequency of about 2 Hz; cross-shore positions of the shoreline are then converted into run-up levels using the mean slope of the swash zone. In doing this we assume that the sub-aerial beach experiences negligible morphological changes between storm events and holds approximately the same slope across the winter season. Run-up time series are finally processed to single out individual swash events and their spectral energy density $\mathcal{E}(f)$ is evaluated to estimate the significant properties of the swash motion. Significant run-up height S and its components due to infragravity (low frequency) motions S_{IG} and incident (high frequency) waves S_{inc} are evaluated as follows:

$$S = 4\sqrt{\int_{0.001\ \mathrm{Hz}}^{1\ \mathrm{Hz}} \mathcal{E}(f)\,\mathrm{d}f}, \qquad S_{\mathrm{IG}} = 4\sqrt{\int_{0.001\ \mathrm{Hz}}^{0.05\ \mathrm{Hz}} \mathcal{E}(f)\,\mathrm{d}f}, \qquad S_{\mathrm{inc}} = 4\sqrt{\int_{0.05\ \mathrm{Hz}}^{1\ \mathrm{Hz}} \mathcal{E}(f)\,\mathrm{d}f}, \tag{2}$$

where 0.05 Hz is the frequency conventionally used to separate high-frequency and low-frequency bands in wave spectra (Guza & Thornton, 1982; Hughes et al., 2014). The swash spectral centroids f_c, proxy for mean swash frequency, are evaluated as weighted mean of the frequency range $f = (0.001\text{–}1)$ Hz, with the spectral energy density $\mathcal{E}(f)$ as weights.

2.4 Numerical Modelling

XBeach is a process-based numerical model originally designed to simulate hydro-morphological processes on sandy beaches at storm-event scales (Roelvink et al., 2009; McCall et al., 2010) and recently used also to investigate flow properties in laboratory

conditions (Ruffini et al., 2020) and to study the evolution of infragravity waves (e.g., Bertin et al., 2020).

To make up for the lack of *in situ* hydrological data for Sabaudia, numerical simulations of nearshore wave propagation are performed by means of the one-dimensional non-hydrostatic (NH) implementation of XBeach, to calibrate the model against run-up levels from timestack analysis. In XBeach NH all short wave motions are explicitly resolved (Roelvink et al., 2009) and long wave (infragravity) generation and transformation processes are accounted for, which makes the model suitable for studies of low-frequency wave transformation.

2.4.1 Model Set-up

The study cross-shore section (the location of which is highlighted in Figure 1a) is discretized into a 1D profile to be used as morphology input for XBeach. The bathymetric section chosen for the simulation campaign is an eroded wintertime profile typical of the area (Parlagreco et al., 2019, see also Figure 1a), with an array of two sand bars on a mild surf zone beach ($\beta_s \approx 0.01$) and a steeper intertidal beach face with mean slope $\beta_f = 0.04$–0.045. An inner prominent bar at about 2 m depth is located 150 m from the shoreline, while an outer, more subdued bar at 4 m depth is placed about 300 m from the shoreline (Figure 2). The real bathymetry has been surveyed from the emerged beach to 8 m depth, but to ensure that input waves are applied offshore of the "closure depth" to let them adjust to the local bathymetry before reaching the shore, it is artificially extended to a greater depth through a constant slope. Three different maximum offshore depths, subjected to model calibration, are chosen: 10, 12.5, and 15 m (see Section 2.4.2).

The grid is devised to allow for computationally efficient simulations while guaranteeing an adequate spatial resolution for both wave propagation and swash dynamics. A minimum of 30 nodes per wavelength and a minimum resolved wave period of 3.5 s are imposed. The resulting grid has a variable spacing with a maximum $\Delta x = 2.3$ m at the offshore boundary and a minimum $\Delta x = 0.1$ m at the emerged beach.

Bed friction is implemented through use of a dimensionless friction coefficient c_D computed with a Manning formulation: $c_D = gn^2 d^{-1/3}$, where g is gravity acceleration, d is the local water depth, and n is the Manning coefficient in $\mathrm{s/m^{1/3}}$ (Soulsby, 1997).

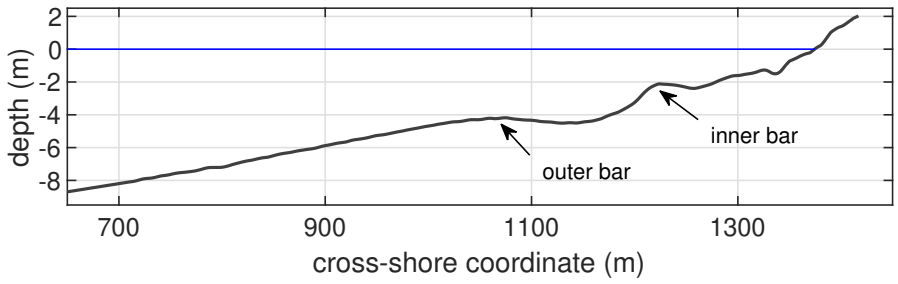

Figure 2. Bathymetric profile used for the simulations. The inner and outer bars are shown. The origin of cross-shore coordinates is placed at the most seaward limit of the profile, where wave input is applied.

Manning's formulation implies a dependence of bed friction on water depth and gives a more realistic condition than Chezy-like (depth-independent) formulations, especially for swash zone processes, for which the typical water depth is usually low. Although the XBeach default value for n is 0.022 s/m$^{1/3}$, model performance is tested with different values of n, representative of beaches ranging from sandy to cobble-made (Benson & Dalrymple, 1967). The sediment transport module of the model is switched off, so that only the hydrodynamics is modelled.

2.4.2 Calibration

We perform a calibration of both physical and operational XBeach parameters. Modelled 2% exceedance wave-induced run-up values $R_{2\%}$ are compared with concurrently observed run-up (extrapolated from timestacks) during eighteen 2-days time windows selected in the period October 2017 – April 2018. The time windows are chosen to encompass a variety of moderate-to-intense wave conditions.

Wave climate boundary conditions for the simulations are imposed at the offshore side of the domain as hourly JONSWAP spectra generated from the wave data extrapolated from the CMEMS hindcast model. The deep-water input parameters (significant wave height H_s and peak period T_p) are shoaled according to the linear wave theory up to one of the three input depths (10, 12.5, or 15 m), according to the simulation. The JONSWAP spectra are automatically varied at the end of each simulated hour (*wbctype = jonstable* in XBeach) to follow the hourly variation of wave climate from CMEMS. This allows for the modelling of time-varying wave conditions within a single simulation.

Calibration is first done on the run-up gauge depth, i.e. the maximum water depth at which the numerical shoreline is detected (*rugdepth* = 0.005, 0.05 and 0.1). At this phase, all other parameters related to physical processes are kept at default values. Afterwards, calibration of the model is performed separately on the parameters representing the maximum value of wave steepness for the onset of wave breaking (*maxbrsteep* = 0.4, 0.6, 0.8) and the Manning friction coefficient (*bedfriccoef* from 0.02 to 0.055, in intervals of 0.005), in the assumption that they are expression of independent processes. Finally, three different offshore profile depths are tested, to account for the possibility of model output to be dependent on the wave input depth. At each step, calibration runs are performed using the optimal value of the parameter from the previous stage. In the calibration process, wave input time series are randomly generated (*random* = 1) to reproduce wave randomness in a natural setting.

Model accuracy in predicting run-up and swash features is evaluated by means of error statistics: MAE (mean-absolute error), bias and the Willmott index of agreement D (Willmott et al., 1985):

$$\text{MAE} = \frac{\sum_{i=1}^{n} |P_i - O_i|}{n}, \tag{3}$$

$$\text{bias} = \frac{\sum_{i=1}^{n} (P_i - O_i)}{n}, \tag{4}$$

$$D = 1 - \frac{\sum_{i=1}^{n} (P_i - O_i)^2}{\sum_{i=1}^{n} \left(|P_i - \bar{O}| + |O_i - \bar{O}| \right)^2} \tag{5}$$

where P_i and O_i are predicted and observed values respectively, $\bar{O}$ is the mean of observed values and n is the number of observations. MAE represents the average error (in absolute value) made by the model, whereas the bias highlights overestimation or underestimation by the model. D is an index of global model performance, with 0 indicating total disagreement between predictions and observations, and 1 indicating total agreement.

2.4.3 Simulation of Sample Storms

The calibrated XBeach is finally employed to model wave transformation for the six sample storms of Table 1, using the same seabed profile employed for the calibration stage (Figure 2). In each simulation, input waves at the offshore boundary are randomly generated from a time-constant JONSWAP spectrum with parameters H_s and T_p as given

in Table 1. The simulated storms last 2 hours (7200 seconds) of run time. Outputs of wave surface elevation and shoreline oscillation are extracted at a sampling frequency of 2 Hz for the second hour of simulation; the first hour is only used as model spin-up and its output is discarded.

The IG fraction of the modelled surface elevation η_{IG} is then extracted from the total wave field η in each simulated storm, by low-pass filtering with a cut-off frequency of 0.05 Hz. A further decomposition of the IG signal into incoming (shoreward, $\eta_{\mathrm{IG,in}}$) and outgoing (seaward, $\eta_{\mathrm{IG,out}}$) components is performed by applying the decomposition method by (Guza et al., 1984), valid for long waves travelling in shallow waters:

$$\eta_{\mathrm{IG,in}} = \frac{1}{2}\left(\eta_{\mathrm{IG}} + u_{\mathrm{IG}}\sqrt{d/g}\right), \qquad \eta_{\mathrm{IG,out}} = \frac{1}{2}\left(\eta_{\mathrm{IG}} - u_{\mathrm{IG}}\sqrt{d/g}\right) \tag{6}$$

where η_{IG} and u_{IG} are the IG surface elevation and depth-averaged cross-shore velocity, respectively.

3 Results

3.1 Real Swash Analysis

Run-up values $R_{2\%}$ extracted with timestack analysis are in good qualitative agreement with the wave climate as hindcast by CMEMS (compare black dots in Figure 3c with the blue line in Figure 3a), which gives preliminary confidence in using synthetic data as input for the calibration of the hydrodynamic model in lack of measured hydrodynamic data. Albeit with some unavoidable scatter due to the comparison of real and synthetic data sets, agreement between modelled wave height H_{s} and resultant swash features is acceptable ($R = 0.67$ for total swash and $R = 0.66$ for swash components and run-up; Figure 3d–g). The distribution of swash spectral centroids f_c (Figure 3h) shows that the mean swash frequency moves towards the low-frequency range as the offshore wave climate intensifies. This is also mirrored by binned and averaged swash spectra (Figure 3i) switching from a double-peak shape for low H_{s}, to single, wide peaks across the IG band for high H_{s}. This is indicative of a transition from a mildly reflective state in weak wave climate, to a distinct dissipative state for intense waves (e.g., see Figure 1 in Hughes et al., 2014). Swash spectra also display a clear f^{-3} roll-off band, indicative of short-wave energy saturation, which extends into the IG band for high H_{s} (Ruessink et al., 1998).

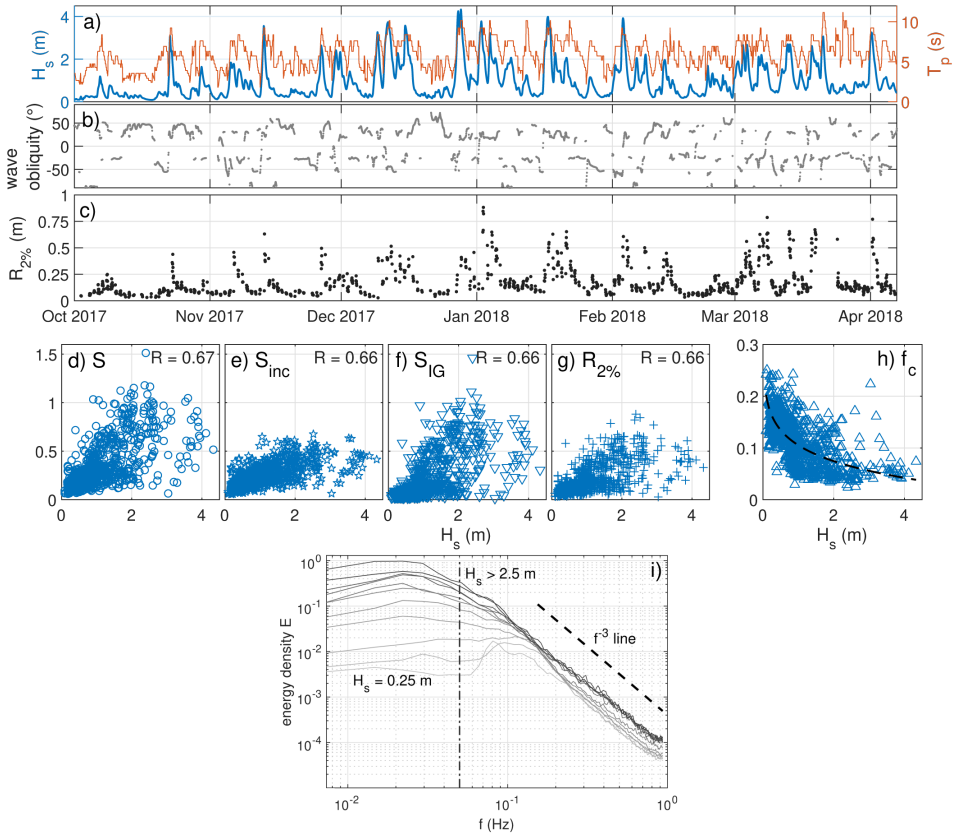

Figure 3. Comparison of wave climate parameters and run-up statistics for the period October 2017 – April 2018: **a)** hindcast significant wave height H_s (blue line, left y-axis) and peak period T_p (orange line, right y-axis); **b)** wave obliquity with respect to the shore normal; **c)** run-up $R_{2\%}$ from timestack analysis. Scatter plots of **d)** significant run-up height S, **e)** incident run-up height S_{inc}, **f)** IG run-up height S_{IG}, **g)** run-up $R_{2\%}$, and **h)** swash centroid frequency f_c against H_s (the best power-law fit is plotted as a dashed line). **i)** Evolution of mean swash spectra for growing H_s. Swash spectra are binned according to offshore H_s into 0.25 m-wide bins and ensemble-averaged. The thin vertical line at 0.05 Hz marks the separation between high-frequency and low-frequency bands. A f^{-3}-slope line is shown for reference.

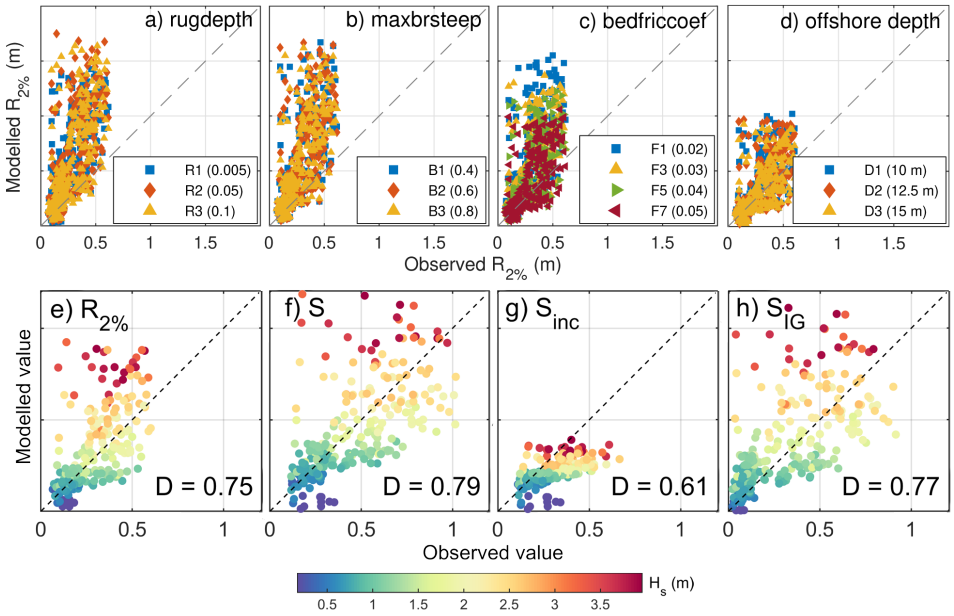

Figure 4. **Top row)** Comparison of modelled vs observed run-up $R_{2\%}$ in the calibration tests, for selected values of **a)** run-up gauge depth, **b)** maximum wave steepness parameter, **c)** Manning friction coefficient, and **d)** offshore profile depth. **Bottom row)** Comparison of modelled vs observed parameters for the fully calibrated model: **e)** run-up $R_{2\%}$, **f)** total swash S, **g)** incident swash S_{inc}, and **h)** infragravity swash S_{IG}. Each dot in panels **e**–**h)** is color-coded according to the offshore H_{s}. Willmott index of agreement D is shown in each plot.

3.2 Model Calibration

Figure 4a–d presents comparison between modelled (XBeach) and observed (timestacks) values of wave-induced run-up $R_{2\%}$ for varying values of the calibration parameters. Figure 4a shows data for varying values of the run-up gauge depth (*rugdepth*) with the other parameters kept at default, and is thus representative of the XBeach performance with no calibration. The default model gives a consistent overestimation of $R_{2\%}$ at all energy levels (maximum bias 0.36 m for test R1, *rugdepth* = 0.005 and minimum bias of 0.32 m for test R3, *rugdepth* = 0.1) and poor performance (D = 0.41 – 0.45). The breaking-related parameter *maxbrsteep* does not significantly improve the model skill (D = 0.44 – 0.45; Figure 4b). On the other hand, the Manning bed friction coefficient *bedfriccoef* is the most influential in tuning model performance. Increasing friction coefficients improves the overall skill (D increasing from 0.49 to 0.72), as well as lowering the positive bias (from 0.29 m to 0.08 m on $R_{2\%}$) and the MAE (from 0.3 m to 0.14 m on $R_{2\%}$;

Figure 4c). Finally, model output is sensitive to offshore water depth: increasing input depths slightly increase the model capability to reproduce on average the observed $R_{2\%}$ (D = 0.72 – 0.75).

The performance of the fully calibrated XBeach model (*rugdepth* = 0.1; *maxbrsteep* = 0.4; *bedfriccoef* = 0.055; offshore depth 15 m) is summarized in Figure 4e–h. The calibrated model, when coupled with hindcast input wave data from CMEMS, is able to reproduce swash features with reasonable accuracy. Modelled run-up $R_{2\%}$ is in good comparison with real values, although an overestimation for high H_s leads to a slightly positive bias ($D = 0.75$, bias = 0.04 m; Figure 4e). Comparison of real and modelled total swash S is also generally good, notwithstanding the scatter due to the coupling of real and synthetic data ($D = 0.79$, bias ≈ 0; Figure 4f). Predicted values of S_{inc} show the least agreement with the observed data; this is mainly due to the model generally underpredicting swash excursion in the incident frequency range, leading to a negative bias across the whole data set ($D = 0.61$, bias = -0.08 m; Figure 4g). On the other hand, the model shows a good performance in modelling the low-frequency swash component S_{IG}, albeit slightly overestimating the real values, in particular for energetic wave conditions ($D = 0.77$, bias = 0.06 m; Figure 4h).

3.3 Wave Transformation Patterns for Sample storms

The calibrated XBeach is employed to model the six sample storms given in Table 1. Figure 5a–c shows the modelled evolution of significant wave height H_s, IG component $H_{s,IG}$, and breaking regions for the sample storms. The percent of breaking time in Figure 5c is calculated as the fraction of the total simulation time for which a breaking wave is registered at a given cross-shore location. We take this parameter as a proxy for the presence of broken waves and to identify the surf zone.

Waves from the three least intense events (S1 to S3, $H_s < 1.3$ m) do not appear to break at the inner bar ($x = 1220$ m; Figure 5c) albeit a drop in wave height is nonetheless modelled shoreward of it. The same events register a cross-shore increase in the IG fraction of wave height $H_{s,IG}$ across the shoaling phase (Figure 5b) simultaneously with a reduction of H_s. A mild rise and fall in $H_{s,IG}$ over the most prominent bar is observed for S3 (Battjes et al., 2004), whereas the growth rate for S1 and S2 is globally monotonic. Since breaking is modelled very close to the shoreline, this implies a gradual energy trans-

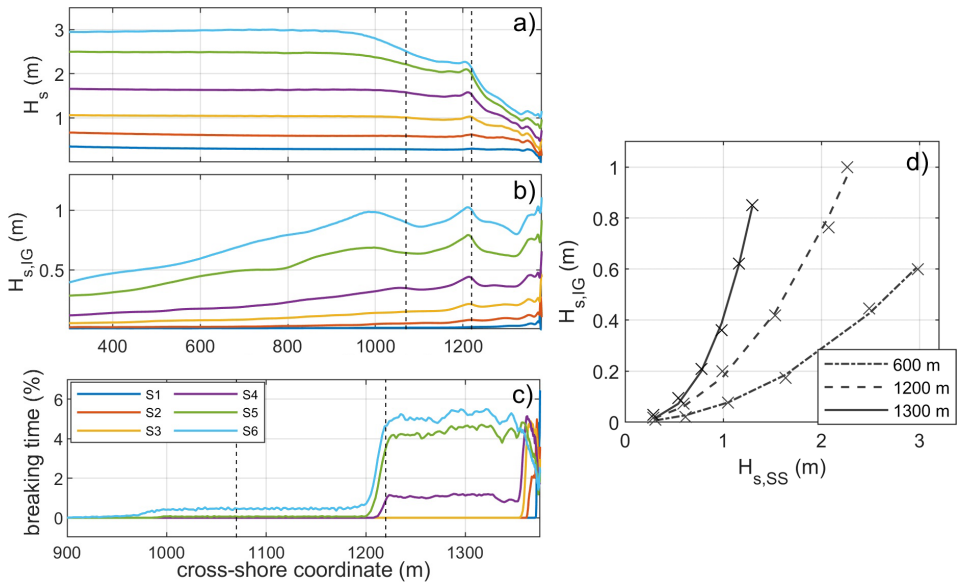

Figure 5. Modelled cross-shore evolution of **a)** significant wave height H_{s}, **b)** IGW height $H_{\mathrm{s,IG}}$, and **c)** surf zones width for the six sample storms. The grey dashed lines mark the crests of the inner bar (x = 1220 m) and outer bar (x = 1070 m). **d)** Relation between significant short wave height $H_{\mathrm{s,SS}}$ and IGW height $H_{\mathrm{s,IG}}$ at three cross-shore locations: x = 600 m (shoaling zone), 1200 m (seaward of the inner bar) and 1300 m (shoreward of the inner bar). Lines give best fits.

fer from short-wave to IG frequencies by shoaling. On the other hand, events S4 to S6 ($H_s > 1.8$ m) exhibit variable breaking frequency over the main bar. The most intense event S6 displays breaking even seaward of the subdued outer bar, starting at around $x = 950$ m. Such evidence places the inner bar at the seaward boundary of the surf zone during intermediate storms and well into the surf zone for the more intense sea states.

Modelled values of the short wave height $H_{s,SS}$ and IGW height $H_{s,IG}$ for specific cross-shore locations are shown in Figure 5d, along with best fitting power-law correlations ($H_{s,IG} = a\,H_{s,SS}^{b}$). Both in the shoaling zone ($x = 600$ m) and seaward of the inner bar ($x = 1200$ m) the power-law correlation is very close to the quadratic relation observed in field studies (Baldock & Huntley, 2002), with $b = 1.97$ and $b = 2.07$ respectively. However, shoreward of the breakpoint and into the surf zone ($x = 1300$ m) the model still gives a more-than-linear relationship with an increased exponent ($b = 2.8$), implying that IG motions are dominant in the surf zone, as also observed on a barred beach by Ruessink (1998).

Modelled patterns of total waves η and IGW ($\eta_{IG,in}$ and $\eta_{IG,out}$) for three sample storms of increasing intensity are finally shown in Figure 6. IGW already present at the shoaling phase reach the surf zone with minimal changes in signal speed upon crossing the bars and entering smaller depths (Figure 6b,e,h). Local enhancement of the highest IG peaks and lowest IG troughs over the inner bar ($x = 1220$ m) is seldomly modelled; this is particularly evident for intermediate wave climate as shown by the intensification of red and blue hues upon crossing the inner bar in Figure 6e. IG signals are eventually reflected at the shoreline (Figure 6c,f,i) and no generation of seaward IGW at the breaking region, signature of BFLW (Moura & Baldock, 2018), is registered.

3.4 IGW as Group Bound Long Waves

IGW at Sabaudia are predominantly present as BLW as suggested by the more-than-linear relationship between IG and short waves (Figure 5d) and the absence of seaward-directed long waves generated at the breakpoint (Figure 6). We here focus on BLW features using data from the modelled sample storms.

As the wave train shoals, its IG content is carried as BLW (Longuet-Higgins & Stewart, 1964) in anti-phase with the short wave envelope ξ (Bertin et al., 2018). Cross-correlation between BLW and ξ at any given location in the shoaling zone should therefore yield neg-

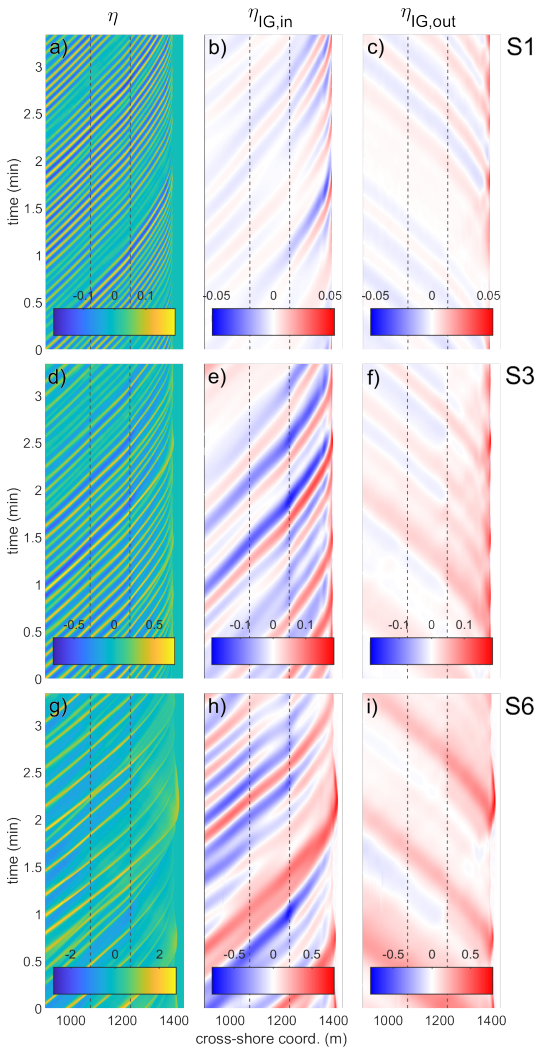

Figure 6. **(a,d,g)** modelled total surface elevation η, **(b,e,f)** shoreward IG component $\eta_{\mathrm{IG,in}}$, and **(c,f,i)** seaward IG component $\eta_{\mathrm{IG,out}}$ for sample storms S1 (top row), S3 (middle row) and S6 (bottom row). Dashed black lines mark the locations of the inner and outer bars.

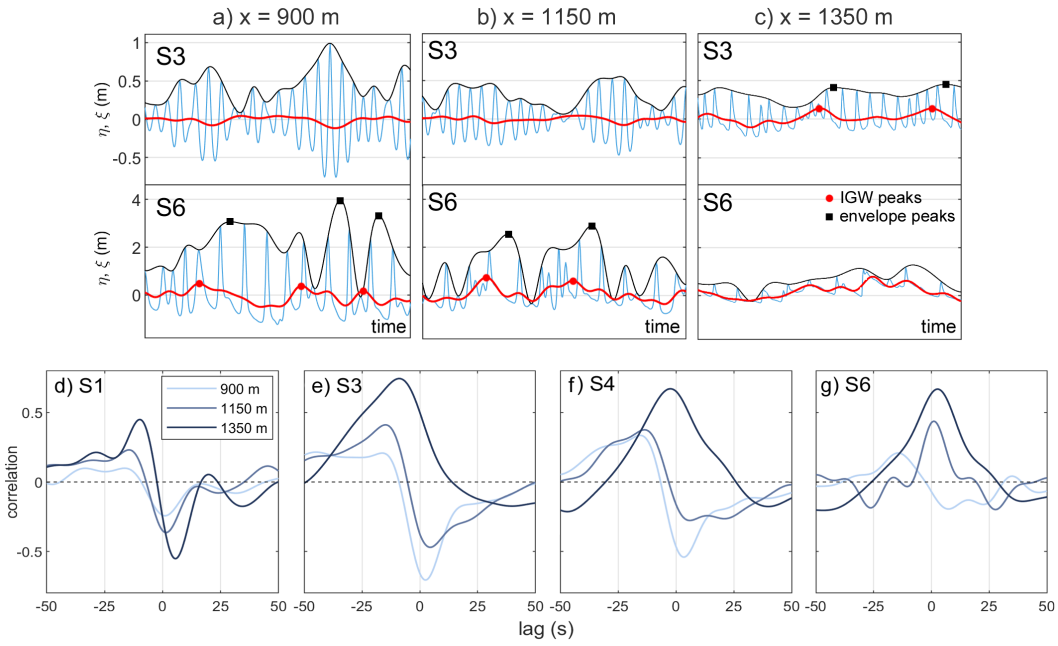

Figure 7. **(a–c)** Snapshots of wave trains η (light blue lines), short wave envelopes ξ (black lines) and underlying IGW η_{IG} (red lines) for sample storms S3 and S6 at three cross-shore locations: x = 900, 1150, and 1350 m. IGW peaks are marked with red circles; envelope peaks are marked with black squares. **(d–g)** ξ–η_{IG} correlations for sample storms S1, S3, S4 and S6 at the same locations.

ative peaks at near-zero lags (Moura & Baldock, 2017). Upon entering smaller depths, the BLW experiences a phase shift and lags behind the wave group as it receives energy from the short waves (Battjes et al., 2004), giving negative correlation peaks at positive lags. Finally, especially for the highest waves and upon breaking, positive surges preceding the BLW trough may occur due to an excess of momentum flux. These surges appear as positive ξ–η_{IG} correlation peaks at negative lags (Moura & Baldock, 2017).

Figure 7d–g illustrates ξ–η_{IG} correlations for four sample storms at three cross-shore locations. In the shoaling zone ($x = 900$ m; light blue lines) negative peaks at zero or near-zero lags suggest that BLW are still bound to the wave envelope. For the most intense storms (Figure 7f–g) mild positive correlations at negative lags ($\approx$ 15 s) are related to a positive surge preceding the trough of the BLW (asymmetric bound wave as in Moura and Baldock (2017)) and a phase shift, required for the energy transfer from short waves to take place (Battjes et al., 2004). Both mechanisms are visible, e.g., in the time series of water elevation for event S6 at $x = 900$ m, in which positive surges and troughs respectively predate and follow the envelope peak (Figure 7a).

A change in correlation patterns occurs at the trough seaward of the inner bar ($x =$ 1150 m; medium blue lines), which corresponds to outer surf zone for the most intense storms (S4 to S6) and inner shoaling zone for the other storms. ξ–η_{IG} correlation is here positive at near-zero lag for storms S4 and S6, suggesting that either the BLW is now in phase with the short wave group, or the IGW is no longer bound to the group and is propagating at the group velocity of the residual wave groups. Mildest waves, which have not yet entered the breaking region at this location, still hold a negative correlation (Figure 7d), whereas intermediate storms (S3–S4; Figure 7e–f) begin to show a marked N-shaped correlation pattern (leading surge and lagging trough), much like storm S6 exhibited in the shoaling zone.

Just seaward of the swash zone ($x = 1350$ m; dark blue lines) only the mildest event S1 still exhibits a N-shaped correlation pattern typical of an asymmetric bound wave.

In conclusion, BLW appear in the wave packet for all storm events in the shoaling zone. For the most intense storms, also a leading surge is identified through cross-correlation patterns. Upon entering the surf zone, the correlation quickly shifts to positive (with small or zero lags), except for the mildest event, for which the breaking pro-

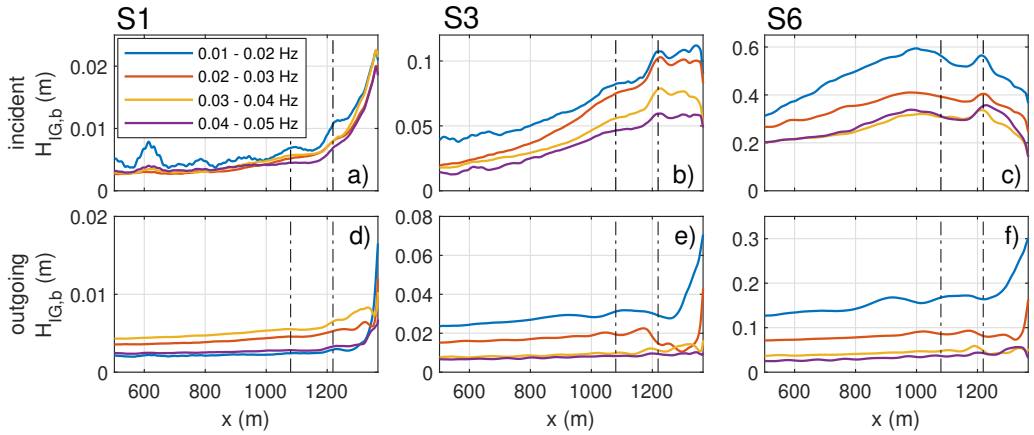

Figure 8. **(a–c)** frequency-dependent incident IGW height and **(d–f)** outgoing IGW height for sample storms S1, S3, and S6. Dashed vertical lines mark the crests of the inner bar ($x = 1220$ m) and outer bar ($x = 1070$ m). Please note the different scales for the vertical axes.

cess occurs very close to the shoreline and no clear signal of released BLW is apparent while shoaling.

3.5 Frequency Dependence of IGW and Tide Effects

To assess a frequency dependence of infragravity processes, the heights of incident and outgoing IGW are calculated for 0.01 Hz-wide bands in the IG range. Results are given in Figure 8. The incoming IG height (Figure 8a–c) displays more or less pronounced maxima over the inner bar and, for the most intense event S6, also seaward of the outer bar. These enhancements are the same in magnitude across all IG bands, implying that the IG response to reducing depths over the bar is frequency-independent in our case. For outgoing (reflected) IGW (Figure 8d–f) maxima over bars are not apparent, as also observed by Battjes et al. (2004). The modelled decrease of IG heights shoreward of the inner bar, especially for more energetic events, has been linked to the release of BLW as the main source of IG oscillations across a barred profile (Ruessink, 1998).

Differences between frequency bands arise when IG reflection patterns at the beach face are investigated by means of the amplitude reflection coefficients R^2 across the surf zone and near the shoreline (Sheremet et al., 2002). R^2 close to 1 indicate strong reflection at the shore, generally associated to a steep beach face and small IG dissipation in the inner surf zone. Small R^2, conversely, denote less IG reflection, by either dissipation

of low-frequency waves across the surf zone or through swash processes over a gentle swash zone. R^2 is defined as the ratio between outgoing (F^-) and incoming (F^+) low-frequency energy fluxes:

$$R^2 = \frac{F^-}{F^+}. \tag{7}$$

F^+ and F^- for the whole IG band ($f < 0.05$ Hz) and for specific 0.01 Hz-wide sub-bands are evaluated from modelled cross-shore fields of detrended water surface elevation η and flow velocity u at any given cross-shore location, by applying the co-located method by Sheremet et al. (2002):

$$F^{\pm} = \int_{f_{\min}}^{f_{\max}} \mathcal{F}^{\pm}(f)\,\mathrm{d}f, \tag{8}$$

$$\mathcal{F}^{\pm}(f) = \frac{\sqrt{gh}}{4}\left\{\mathcal{C}_{\eta\eta}(f) \pm 2\sqrt{\frac{h}{g}}\,\mathcal{C}_{\eta u}(f) + \frac{h}{g}\mathcal{C}_{uu}(f)\right\}, \tag{9}$$

where $[f_{\min}\ f_{\max}]$ is the frequency range over which the fluxes $\mathcal{F}^{\pm}(f)$ are to be integrated, $\mathcal{C}_{\eta\eta}$ and $\mathcal{C}_{uu}$ are the water elevation and flow velocity autospectra, respectively, and $\mathcal{C}_{\eta u}$ is the η–u cospectrum, i.e. the real part of the η–u cross-spectrum. Bulk IG reflection coefficients are evaluated by integrating the fluxes over the whole IG band, while band-specific coefficients are integrated across 0.01 Hz-wide sub-bands.

Figure 9 shows the distribution of modelled fluxes $F^{\pm}$ and IG reflection coefficients R^2 for two sample storms of different intensity, representative of mild and intense wave climate, at conditions of low and high tide. $F^{\pm}$ and R^2 are evaluated by means of equations (7–9) at a set of cross-shore locations in the inner surf zone (up to about 70 m seaward from the mean still-water shoreline). To compare low- and high-tide observations in a single reference frame, all data are plotted as a function of the distance from the respective shoreline. Bulk reflection is generally high in the innermost portion of the surf zone ($R^2 > 0.5$ at 10–20 m from the shoreline, $d \leq 1$ m) and decays seaward with stronger gradients for mild than for intense wave climate (Figure 9c,d). The lowest IG frequencies, $f < 0.01$ Hz, experience the largest reflection (Figure 9e,h) with surf zone R^2 consistently over 0.5 for the mild event S2 and over 0.7 for energetic event S5. As the IG frequency increases towards the short-wave range, the modelled reflection coefficients decrease and eventually become negligible, indicating increasingly dominant dissipation at the shore (Figure 9g,j). Although showing similar trends, incoming fluxes F^+ are larger

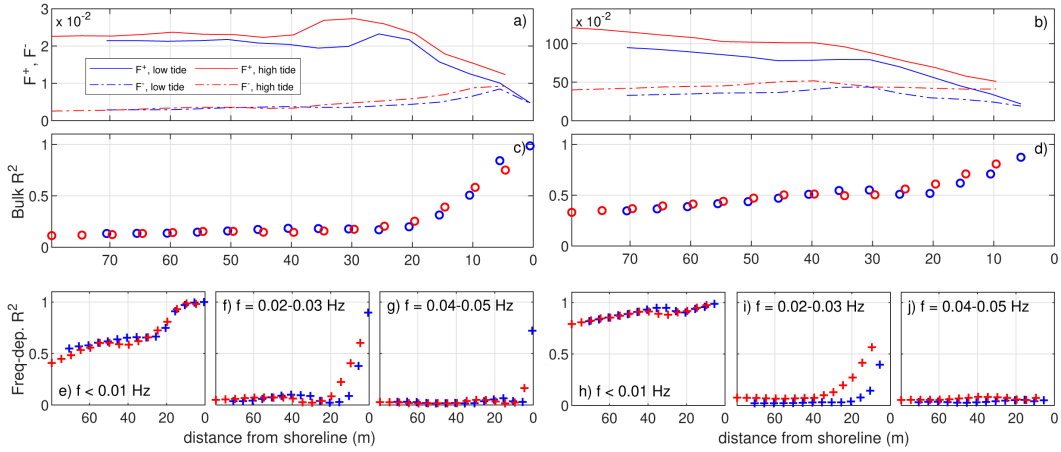

Figure 9. **(a,b)** modelled inner surf zone evolution of incoming (F^+, solid lines) and outgoing IG fluxes (F^-, dash-dotted lines); **(c,d)** bulk IG reflection coefficients R^2; **(e–j)** frequency-dependent IG reflection coefficients, for sample storms S2 (left panels) and S5 (right panels), at low tide (MLWS = −0.2 m; blue lines and symbols) and high tide (MHWS = +0.2 m; red lines and symbols). Please note the different scales for the fluxes in panels **(a,b)**.

at high tide than at low tide (Figure 9a,b) due to slightly larger water depths contributing in reducing energy losses from frictional dissipation and/or wave breaking. Tidal modulation of F^+ is also mirrored by different levels of offshore F^-, even though with intense wave climate only, as observed also by Thomson et al. (2006).

4 Discussion

4.1 Hindcast Data as Input for Numerical Modelling

In the present work we have explored the possibility of using hindcast data from the oceanographic service CMEMS as input for the calibration of XBeach against observed swash properties. Wave data from CMEMS have been previously used to study sandbar displacement patterns with good results (Melito et al., 2020).

Good correspondence between hindcast wave climate and real swash properties across a six-month period (R = 0.66–0.67) supports use of data from CMEMS in conjunction with XBeach for swash modelling. However, even after calibration, some scatter is observed between modelled (obtained by XBeach using hindcast wave parameters as input) and real swash features. This is all the more apparent for S and S_{IG} (Figure 4f and h) and results in moderate mean errors of 0.16 m for S_{IG} and 0.15 m for S, respectively.

The source of this error mainly lies in the not always exact correspondence between modelled climate and real swash features.

Calibration has been made upon swash properties, which are the final product of a series of complex hydrodynamic processes (shoaling, breaking, frictional energy loss) taking place across the surf zone. It is likely that further calibration on hydrodynamic parameters would yield a better, physically grounded model tuning and reduce errors.

4.2 Model Performance

For the first time to the best of the authors' knowledge, an approach for model calibration using swash-related processes has been proposed to make up for the lack of directly measured hydrodynamic data. This method exploits standard products from video-monitoring facilities and is suitable when model calibration is desired but deployment of *in situ* instrumentation is troublesome, not economically convenient or impossible.

The 1D version of the non-hydrostatic XBeach with default parameters overestimates wave-induced run-up $R_{2\%}$, with the highest overestimation occurring for high-energy conditions (Figure 4a), as observed also by Stockdon et al. (2014). As expected, friction is shown to have a major influence on improving average model performance (Conde-Frias et al., 2017), with higher Manning coefficients acting by reducing modelled $R_{2\%}$ as well as the overall bias. The run-up gauge depth, on the other hand, has limited impact on modelled $R_{2\%}$, although the best results are attained with a value of 0.1 m, significantly higher than the default value of 0.005 m. This observation is consistent with other studies (Stockdon et al., 2014; Fiedler et al., 2015; Pinault et al., 2020) which used the same value to extract run-up from lidar timestacks and numerically modelled swash.

A negative bias for S_{inc} (-0.08 m) means a global underprediction of incident swash and might suggest that the default wave dissipation formulation implemented in XBeach gives an energy dissipation higher than that observed in the field, irrespective of tuning parameters. The model also shows a clear saturation value of about 0.45 m for S_{inc} (Figure 4g) and less scattering around the respective observed values, although the saturation value for S_{inc} is higher for observed swash motions (0.8 m). On the other hand, modelled IG swash S_{IG} shows virtually no sign of saturation (Figure 4h), as confirmed also by growing energy in the IG range from remotely sensed swash spectra, except for the

most intense waves for which the highest IG frequencies experience incipient saturation (Figure 3e).

Less scattering and overall better skill for predictions of $R_{2\%}$ than for S and S_{IG} (Figure 4) lend support to the choice of $R_{2\%}$ as the optimal parameter to be taken as output from numerical models when forced by synthetic input data from oceanographic models, since its value is less influenced by individual waves than swash-related statistics are, at least in a long-term simulation.

4.3 IGW Transformation

IGW at Sabaudia are dominated by BLW, as commonly observed on gently sloping beaches (Battjes et al., 2004; Baldock, 2012). Long waves are seen to grow in intensity with all wave conditions as gravity waves undergo shoaling, with amplification ratios higher for milder waves (Figure 6). Upon reaching the surf zone and shoreline, their presence and intensity are still relevant to the point of quickly overcoming short-wave wave energy. The IG height $H_{\mathrm{s,IG}}$ is indeed in quadratic dependence from the incident short wave height $H_{\mathrm{s,SS}}$ in the shoaling phase (Figure 5d; see also Baldock & Huntley, 2002); in contrast with, e.g., Moura and Baldock (2017), however, such relationship is conserved in the surf zone, denoting that IGW experience little dissipation immediately after short wave breaking. This also highlights the irrelevance of breakpoint forcing, which is conversely dominant on steeper beaches, $\beta_s \approx 0.01$ or higher (Baldock et al., 2000; Pomeroy et al., 2012), especially when combined with steep waves.

IGW growth stops upon reaching the inner bar for intermediate states and also the outer, subdued bar for the most energetic states (Figure 8b). The regions of IGW stationarity/decay are consistent with the identification of surf zones made through identification of wave breaking regions (Figure 5), suggesting that the energy transfer from gravity waves to lower subharmonics, apparent during shoaling, is interrupted in the surf zone (Battjes et al., 2004). The release of previously bound low-frequency content during or immediately after breaking is signaled by the IG components η_{IG} being no more in phase opposition with the short wave envelope ξ when reaching the respective surf zones (Figure 7). Interestingly, ξ–η_{IG} correlations are seen to switch to positive (BLW release) while still into the inner shoaling zone for intermediate wave conditions, in contrast with the concept that BLW release is linked to wave breaking and groupiness destruction. More-

over, the correlation shifting from negative peaks to N-shapes or positive peaks (at zero or negative lags) as waves approach and enter the surf zone (Figure 7e–g) highlights the development of an asymmetric wave with a leading positive elevation as a result of dynamic setup. Our study thus confirms the presence of asymmetric IGW in the surf zone also in mild, barred beaches, much similarly to what laboratory evidence (Baldock, 2006) and numerical modelling (Pomeroy et al., 2012) have previously observed on steep beaches and reefs.

Dissipation by IGW breaking appears to be the dominant energy draining process for intermediate and intense wave states, as suggested by the decay of IG heights in the surf zone (Figure 8b–c), where the typical cross-shore distances are too short for seabed friction dissipation to be effective. This assumption is corroborated by still rather high IGW heights, reaching as much as 1 m before the shoreline (Figure 5); IG wave heights of similar magnitude have been also reported by Guza and Thornton (1982) and Ruessink et al. (1998) among others. Breaking dissipation in shallow waters (0.7 m) and short distances (25–55 m), likely promoted by IGW breaking seaward of the shore, is also observed at the similarly sloped beach of Ameland by de Bakker et al. (2014).

High values of R^2 at the shallowest region, up to 10 m from the shoreline (Figure 9c,d) and the growing relevance of IG energy in real swash spectra (Figure 3i) suggest that localized IG dissipation at the shoreline, by either swash interactions or depth-limited dissipation, may be limited; however, the modelled decay pattern of surf zone IGW heights for the moderately intense events (Figure 8b–c) is consistent with that obtained by SWASH simulations with a friction coefficient $c_f = 0.005$ in de Bakker et al. (2014), therefore we cannot completely rule out the effect of seabed friction into IGW dissipation. The data in our study, unfortunately, does not allow us to further inspect the influence of dissipation mechanisms. A more complete understanding of the processes at hand would benefit from a collection and analysis of field observations.

4.4 Frequency and Tide Dependence of IGW Processes

Several studies have ascertained that the cross-shore transformation of low-frequency oscillations is a function of wave frequency (e.g., Battjes et al., 2004; van Dongeren et al., 2007; de Bakker et al., 2014).

In Sabaudia, differences between IG bands are found mainly for moderate-to-strong wave conditions, with the lowest IG frequencies presenting the largest incident wave heights (Figure 8b,c) as well as the largest reflection (Figure 9d,h), while the higher IG frequencies are characterized by smaller heights and lower reflection. This behaviour is connected with enhanced near-shoreline dissipation experienced by higher IG frequencies, since swash energy saturation (typical of gravity waves in the swash zone of a mild sloping beach) reaches the higher IG frequencies as wave climate intensifies (Figure 3i). Weak wave climate, on the other hand, yields a continuous growth of low-frequency oscillations up to the shoreline at all frequencies, likely due to the limited influence of wave breaking and seabed dissipation, and still non-negligible reflection at the lowest frequencies (Figure 9e).

A modified version of the dimensionless normalized bed slope (Battjes et al., 2004), developed with a focus on infragravity frequencies, can be profitably used to discuss dissipation and reflection of IGW in very shallow waters (van Dongeren et al., 2007; de Bakker et al., 2014):

$$\beta_{\mathrm{H}} = \frac{d_x}{2\pi f_{\mathrm{IG}}} \sqrt{\frac{g}{H_{\mathrm{IG}}}} \tag{10}$$

where d_x is the bed slope, f_{IG} is the IG wave frequency, H_{IG} is the incoming IGW height at a given point close to the shore. Using β_{H}, two regimes can be distinguished (Battjes et al., 2004): (i) a *steep-slope regime*, in which IGW experience little-to-no dissipation and considerable reflection occurs at the shore, and (ii) a *mild-slope regime*, where IGW dissipation is more consistent, likely due to breaking of IG bores very close to the shore.

Our findings mark a difference from the literature also in regards of regime transition. Normalized bed slopes evaluated at $x = 1350$ m ($d = 0.75$ m, mean bed slope of 0.04) give values of 3.22–9.25 across all IG bands for the mildest event S1, which indeed presents a steep-slope behaviour with virtually no dissipation of the incoming IG energy (Figure 8a,d). At the opposite side of the spectrum, $\beta_{\mathrm{H}} = 0.94$–$2.05$ are predicted for the most energetic event S6, presenting a distinct mild-slope regime with consistent IG dissipation onshore of the inner bar for all frequency bands ($x > 1200$ m; Figure 8c,f). The intermediate state S3 shows a combination of features: shoaling of IG waves up to the inner bar and stationarity shoreward of it (Figure 8b and e). This case lies in the transition range between the two regimes and yields $\beta_{\mathrm{H}} = 1.83$–$3.98$; such range of values is higher than classical thresholds identified through analysis of experimental data,

β_H ≈1–1.25 (Battjes et al., 2004; van Dongeren et al., 2007). Our findings thus go in favour of the concept of regime transition occurring for values of β_H higher than those suggested by the literature. In fact, our result is more compatible with the tentative threshold $\beta_H \approx 3$ suggested by de Bakker et al. (2014) and found for a slope of 0.0125.

Although in a distinctly microtidal environment, the effect of tide is apparent in altering onshore energy fluxes and reflection coefficients, mainly for intermediate IG frequencies ($f = 0.02 - 0.03$ Hz; Figure 9f,i). Those frequencies are at the transition between a steep-slope regime with predominant reflection (low IG frequencies) and a mild-slope regime, where dissipation is dominant (high IG frequencies), so tidal excursion is effective in shifting the boundary between the almost complete reflection at lowest IG, and the dominant dissipation at highest IG, even though the tide is not seen to exert a significant influence on the bulk IGW reflection (Figure 9c,d). Specifically, low tide reduces reflection of the intermediate IG mainly by reducing F^+ close to shore (thus shifting the beach behaviour towards a mild-slope regime for that frequency band) and leaving much less energy to reach to shoreline and be reflected (Thomson et al., 2006). Although different in value, decreasing rates of F^+ are similar in high tide and low tide (Figure 9a,b), due to almost equal surf zone and intertidal beach slopes at high and low tide.

5 Conclusions

A numerical analysis of generation and transformation of low-frequency waves at the dissipative, microtidal beach of Sabaudia (Tyrrhenian Sea, Italy) has been proposed. IG evolution patterns originating from a range of wave conditions and tidal stages are investigated. The study contributes to increase our understanding of IGW properties in microtidal environments, which have been comparatively less studied than meso- and macrotidal coasts in this regard.

XBeach has been subjected to a novel, feasible calibration process against field observations of run-up and swash characteristics from a nearby monitoring station, with hindcast data from a basin-scale oceanographic model as wave input. The calibrated model is shown to model swash features with reasonable skill, although scatter is observed due to congenital discrepancies between the synthetic wave climate and the real swash regime.

A dominance of BLW at the dissipative beach of Sabaudia, especially with intense wave conditions, has been observed. A steady growth of IGW heights is modelled across

the shoaling zone for both low and high wave energy conditions, consistently with a global transfer of wave energy towards the lower frequency by the action of radiation stress. The release of BLW, however, is not necessarily linked to wave breaking as commonly assumed, as hints of BLW release are observed prior to the inception of wave breaking (inner shoaling zone) for intense wave states. IGW stop growing upon entering the surf zone mostly as free waves and are predominantly dissipated by breaking in shallow waters, while friction-based dissipation is considered negligible.

Analysis of frequency-dependent IGW heights as a function of storm intensity shows a clear transition from a mild-slope regime, with strong amplification and virtually no dissipation of IGW in weak wave climate, to a steep-slope behaviour with non-negligible IG dissipation in a 400 m-wide region extending well seaward of the outer bar. Such transition, moreover, occurs at higher β_H than expected. When only the intermediate IG frequencies are accounted for, however, low tide is able to shift the beach behaviour towards a mild-slope regime (reduced R^2) by reducing onshore energy fluxes.

Our study gives first evidence that the tide is able to exert control over dissipation regimes of a mild sloping beach even in coasts with a small tidal excursion (up to 0.5 m); we thus suggest considering also tidal excursion when analyzing dynamics for which the energy of low-frequency motions is known to be important, e.g. sediment mobilization and coastal inundation at gently sloping beaches.

Acknowledgments

This study is funded by Circeo National Park and Gargano National Park within the National Biodiversity Strategy promoted by the Ministero dell'Ambiente e della Tutela del Territorio e del Mare (MATTM), Italy (GAB0024444). Financial support from the Office of Naval Research Global (UK) MORSE Project (Research Grant Number N62909-17-1-2148) and the MIUR PRIN 2017 Project, Italy "FUNdamentals of BREAKing wave-induced boundary dynamics – FUNBREAK" (Grant Number 20172B7MY9) is gratefully acknowledged. Inputs and datasets used for the calibration process and sample storms simulation are available at the following Zenodo repository: `https://doi.org/10.5281/zenodo.5470254`

References

Aagaard, T., & Holm, J. (1989). Digitization of wave run-up using video records. *Journal of Coastal Research*, 547–551.

Baldock, T. (2006). Long wave generation by the shoaling and breaking of transient wave groups on a beach. *Proceedings of the Royal Society A: Mathematical, Physical and Engineering Sciences*, *462*(2070), 1853–1876. doi: 10.1098/rspa.2005.1642

Baldock, T. (2012). Dissipation of incident forced long waves in the surf zone—Implications for the concept of "bound" wave release at short wave breaking. *Coastal Engineering*, *60*(1), 276–285. doi: 10.1016/j.coastaleng.2011.11.002

Baldock, T., & Huntley, D. (2002). Long-wave forcing by the breaking of random gravity waves on a beach. *Proceedings of the Royal Society A: Mathematical, Physical and Engineering Sciences*, *458*(2025), 2177–2201. doi: 10.1098/rspa.2002.0962

Baldock, T., Huntley, D., Bird, P., O'hare, T., & Bullock, G. (2000). Breakpoint generated surf beat induced by bichromatic wave groups. *Coastal Engineering*, *39*(2–4), 213–242.

Baldock, T., Manoonvoravong, P., & Pham, K. S. (2010). Sediment transport and beach morphodynamics induced by free long waves, bound long waves and wave groups. *Coastal Engineering*, *57*(10), 898–916.

Battjes, J. A. (1974). Surf similarity. In *Coastal engineering proceedings* (pp. 466–480). doi: 10.9753/icce.v14.26

Battjes, J. A., Bakkenes, H. J., Janssen, T. T., & van Dongeren, A. R. (2004). Shoaling of subharmonic gravity waves. *Journal of Geophysical Research: Oceans*, *109*(C2). Retrieved from `https://agupubs.onlinelibrary.wiley.com/doi/abs/10.1029/2003JC001863` doi: https://doi.org/10.1029/2003JC001863

Benson, M. A., & Dalrymple, T. (1967). *General field and office procedures for indirect discharge measurements* (Tech. Rep.). Retrieved from `http://pubs.er.usgs.gov/publication/twri03A1` doi: 10.3133/twri03A1

Bertin, X., de Bakker, A., van Dongeren, A., Coco, G., André, G., Ardhuin, F., ... Tissier, M. (2018). Infragravity waves: From driving mechanisms to impacts.

Earth-Science Reviews, *177*, 774–799. doi: 10.1016/j.earscirev.2018.01.002

Bertin, X., Martins, K., Bakker, A., Chataigner, T., Guérin, T., Coulombier, T., & Viron, O. (2020). Energy Transfers and Reflection of Infragravity Waves at a Dissipative Beach Under Storm Waves. *Journal of Geophysical Research: Oceans*, *125*(5). doi: 10.1029/2019JC015714

Bertin, X., & Olabarrieta, M. (2016). Relevance of infragravity waves in a wave-dominated inlet. *Journal of Geophysical Research: Oceans*, 5418–5435. doi: 10.1002/2015JC011444

Conde-Frias, M., Otero, L., Restrepo, J. C., Ortiz, J. C., Ruiz, J., & Osorio, A. F. (2017). Swash Oscillations in a Microtidal Dissipative Beach. *Journal of Coastal Research*, *33*(6), 1408–1422. doi: 10.2112/JCOASTRES-D-16-00147.1

de Bakker, A. T., Tissier, M. F., & Ruessink, B. G. (2014). Shoreline dissipation of infragravity waves. *Continental Shelf Research*, *72*, 73–82. doi: 10.1016/j.csr.2013.11.013

de Bakker, A. T., Brinkkemper, J. A., van der Steen, F., Tissier, M. F., & Ruessink, B. G. (2016). Cross-shore sand transport by infragravity waves as a function of beach steepness. *Journal of Geophysical Research: Earth Surface*, *121*(10), 1786–1799. doi: 10.1002/2016JF003878

Fiedler, J. W., Brodie, K. L., McNinch, J. E., & Guza, R. T. (2015, nov). Observations of runup and energy flux on a low-slope beach with high-energy, long-period ocean swell. *Geophysical Research Letters*, *42*(22), 9933–9941. Retrieved from `http://doi.wiley.com/10.1002/2015GL066124` doi: 10.1002/2015GL066124

Guza, R. T., & Thornton, E. B. (1982). Swash oscillations on a natural beach. *Journal of Geophysical Research*, *87*(C1), 483–491. doi: 10.1029/jc087ic01p00483

Guza, R. T., Thornton, E. B., & Holman, R. A. (1984). Swash on steep and shallow beaches. *Coastal Engineering Proceedings*, *1*(19), 48. doi: 10.9753/icce.v19.48

Holman, R. A., Sallenger, A. H., Lippmann, T. C., & Haines, J. W. (1993). The application of video image processing to the study of nearshore processes. *Oceanography*, *6*(3), 78–85.

Hughes, M. G., Aagaard, T., Baldock, T. E., & Power, H. E. (2014). Spectral signatures for swash on reflective, intermediate and dissipative beaches. *Marine Geology*, *355*, 88–97. Retrieved from `https://linkinghub.elsevier.com/`

retrieve/pii/S0025322714001492 doi: 10.1016/j.margeo.2014.05.015

Korres, G., Ravdas, M., & Zacharioudaki, A. (2019). *Mediterranean Sea Waves Hindcast (CMEMS MED-Waves).* Copernicus Monitoring Environment Marine Service (CMEMS). doi: 10.25423/CMCC/MEDSEA_HINDCAST_WAV_006_012

Lippmann, T. C., & Holman, R. A. (1989). Quantification of sand bar morphology: a video technique based on wave dissipation. *Journal of Geophysical Research*, *94*(C1), 995–1011. doi: 10.1029/JC094iC01p00995

Longuet-Higgins, M. S., & Stewart, R. W. (1964). Radiation stresses in water waves; a physical discussion, with applications. *Deep Sea Research and Oceanographic Abstracts*, *11*(4), 529–562. doi: 10.1016/0011-7471(64)90001-4

McCall, R. T., Van Thiel de Vries, J. S. M., Plant, N. G., Van Dongeren, A. R., Roelvink, J. A., Thompson, D. M., & Reniers, A. J. H. M. (2010). Two-dimensional time dependent hurricane overwash and erosion modeling at Santa Rosa Island. *Coastal Engineering*, *57*(7), 668–683. doi: 10.1016/j.coastaleng.2010.02.006

Melito, L., Parlagreco, L., Perugini, E., Postacchini, M., Devoti, S., Soldini, L., ... Brocchini, M. (2020). Sandbar dynamics in microtidal environments: Migration patterns in unprotected and bounded beaches. *Coastal Engineering*, *161*, 103768.

Moura, T., & Baldock, T. (2017). Remote sensing of the correlation between breakpoint oscillations and infragravity waves in the surf and swash zone. *Journal of Geophysical Research: Oceans*, *122*(4), 3106–3122. doi: 10.1002/2016JC012233

Moura, T., & Baldock, T. E. (2018). New Evidence of Breakpoint Forced Long Waves: Laboratory, Numerical, and Field Observations. *Journal of Geophysical Research: Oceans*, *123*(4), 2716–2730. doi: 10.1002/2017JC013621

Okihiro, M., & Guza, R. (1995). Infragravity energy modulation by tides. *Journal of Geophysical Research: Oceans*, *100*(C8), 16143–16148.

Okihiro, M., Guza, R., & Seymour, R. (1993). Excitation of seiche observed in a small harbor. *Journal of Geophysical Research: Oceans*, *98*(C10), 18201–18211.

Parlagreco, L., Melito, L., Devoti, S., Perugini, E., Soldini, L., Zitti, G., & Brocchini,

M. (2019). Monitoring for coastal resilience: Preliminary data from five Italian sandy beaches. *Sensors (Switzerland)*, *19*(8), 1854. doi: 10.3390/s19081854

Pinault, J., Morichon, D., & Roeber, V. (2020). Estimation of irregular wave runup on intermediate and reflective beaches using a phase-resolving numerical model. *Journal of Marine Science and Engineering*, *8*(12), 993. doi: 10.3390/jmse8120993

Pomeroy, A., Lowe, R., Symonds, G., Van Dongeren, A., & Moore, C. (2012). The dynamics of infragravity wave transformation over a fringing reef. *Journal of Geophysical Research: Oceans*, *117*(C11), C11022. doi: 10.1029/2012JC008310

Roelvink, D., Reniers, A., van Dongeren, A., van Thiel de Vries, J., McCall, R., & Lescinski, J. (2009). Modelling storm impacts on beaches, dunes and barrier islands. *Coastal Engineering*, *56*(11-12), 1133–1152. doi: 10.1016/j.coastaleng.2009.08.006

Ruessink, B. G. (1998). The temporal and spatial variability of infragravity energy in a barred nearshore zone. *Continental Shelf Research*, *18*(6), 585–605. doi: 10.1016/S0278-4343(97)00055-1

Ruessink, B. G., Kleinhans, M. G., & van den Beukel, P. G. L. (1998). Observations of swash under highly dissipative conditions. *Journal of Geophysical Research: Oceans*, *103*(C2), 3111–3118. doi: 10.1029/97jc02791

Ruffini, G., Briganti, R., Alsina, J. M., Brocchini, M., Dodd, N., & McCall, R. (2020). Numerical modeling of flow and bed evolution of bichromatic wave groups on an intermediate beach using nonhydrostatic XBeach. *Journal of Waterway, Port, Coastal, and Ocean Engineering*, *146*(1), 04019034.

Ruggiero, P., Komar, P. D., McDougal, W. G., Marra, J. J., & Beach, R. A. (2001). Wave runup, extreme water levels and the erosion of properties backing beaches. *Journal of Coastal Research*, *17*(2), 407–419.

Sheremet, A., Guza, R. T., Elgar, S., & Herbers, T. H. (2002). Observations of nearshore infragravity waves: Seaward and shoreward propagating components. *Journal of Geophysical Research: Oceans*, *107*(8), 3095. doi: 10.1029/2001jc000970

Soldini, L., Antuono, M., & Brocchini, M. (2013). Numerical modeling of the influence of the beach profile on wave run-up. *Journal of Water-*

way, Port, Coastal, and Ocean Engineering, *139*(1), 61–71. doi: 10.1061/(asce)ww.1943-5460.0000163

Soulsby, R. (1997). *Dynamics of marine sands*. Thomas Telford Publishing. doi: 10.1680/doms.25844

Stockdon, H. F., Holman, R. A., Howd, P. A., & Sallenger, A. H. (2006). Empirical parameterization of setup, swash, and runup. *Coastal Engineering*, *53*(7), 573–588. doi: 10.1016/j.coastaleng.2005.12.005

Stockdon, H. F., Thompson, D. M., Plant, N. G., & Long, J. W. (2014). Evaluation of wave runup predictions from numerical and parametric models. *Coastal Engineering*, *92*, 1–11. doi: 10.1016/j.coastaleng.2014.06.004

Symonds, G., Huntley, D. A., & Bowen, A. J. (1982). Two-dimensional surf beat: Long wave generation by a time-varying breakpoint. *Journal of Geophysical Research: Oceans*, *87*(C1), 492–498.

Taramelli, A., Cappucci, S., Valentini, E., Rossi, L., & Lisi, I. (2020, mar). Nearshore sandbar classification of Sabaudia (Italy) with LiDAR data: The FHyL approach. *Remote Sensing*, *12*(7), 1053. doi: 10.3390/rs12071053

Thomson, J., Elgar, S., Raubenheimer, B., Herbers, T. H., & Guza, R. T. (2006). Tidal modulation of infragravity waves via nonlinear energy losses in the surfzone. *Geophysical Research Letters*, *33*(5), L05601. doi: 10.1029/2005GL025514

van Dongeren, A., Battjes, J., Janssen, T., van Noorloos, J., Steenhauer, K., Steenbergen, G., & Reniers, A. (2007). Shoaling and shoreline dissipation of low-frequency waves. *Journal of Geophysical Research: Oceans*(2), C02011. doi: 10.1029/2006JC003701

Website of the Italian Tide Gauge Network. (2021). `https://www.mareografico.it`. (Accessed: September 6, 2021)

Williams, M. E., & Stacey, M. T. (2016). Tidally discontinuous ocean forcing in bar-built estuaries: The interaction of tides, infragravity motions, and frictional control. *Journal of Geophysical Research: Oceans*, *121*(1), 571–585. doi: 10.1002/2015JC011166

Willmott, C. J., Ackleson, S. G., Davis, R. E., Feddema, J. J., Klink, K. M., Legates, D. R., ... Rowe, C. M. (1985). Statistics for the evaluation and comparison of models. *Journal of Geophysical Research*, *90*(C5), 8995–9005.

803 doi: 10.1029/jc090ic05p08995

804 Wright, L. D., & Short, A. D. (1984). Morphodynamic variability of surf zones and
805 beaches: A synthesis. *Marine Geology*, *56*(1-4), 93–118. doi: 10.1016/0025
806 -3227(84)90008-2